

PAPER

## Steerable chromatic dispersive metalenses in dual bands

To cite this article: Boyan Fu *et al* 2022 *J. Phys. D: Appl. Phys.* **55** 255105

View the [article online](#) for updates and enhancements.

### You may also like

- [Final report of EUROMET-PR.S1.1: Bilateral intercomparison on measurements of chromatic dispersion reference fibres between METAS \(Switzerland\) and MIKES \(Finland\)](#)  
Jacques Morel and Antti Lamminpää

- [EUROMET Project 666, EUROMET-PR.S1 Final Report: Intercomparison of chromatic dispersion reference fibres](#)  
Jacques Morel

- [Mid-infrared supercontinuum generation with high spectral flatness in dispersion flattened tellurite all-solid hybrid microstructured optical fibers](#)  
Hoa Phuoc Trung Nguyen, Tong Hoang Tuan, Morio Matsumoto et al.



The Electrochemical Society  
Advancing solid state & electrochemical science & technology

242nd ECS Meeting

Oct 9 – 13, 2022 • Atlanta, GA, US

**Extended abstract submission deadline: April 22, 2022**

Connect. Engage. Champion. Empower. Accelerate.

**MOVE SCIENCE FORWARD**



**Submit your abstract**



# Steerable chromatic dispersive metalenses in dual bands

Boyan Fu<sup>1</sup> , Tianyue Li<sup>1</sup> , Xiujuan Zou<sup>1</sup>, Jianzheng Ren<sup>1</sup>, Quan Yuan<sup>1</sup>, Shuming Wang<sup>1,2,\*</sup> , Xun Cao<sup>1,2</sup>, Zhenlin Wang<sup>1</sup> and Shining Zhu<sup>1,2,\*</sup>

<sup>1</sup> National Laboratory of Solid-State Microstructures, School of Physics, School of Electronic Science and Engineering, Nanjing University, Nanjing 210093, People's Republic of China

<sup>2</sup> Key Laboratory of Intelligent Optical Sensing and Manipulation, Ministry of Education, Nanjing 210093, People's Republic of China

E-mail: [wangshuming@nju.edu.cn](mailto:wangshuming@nju.edu.cn) and [zhusn@nju.edu.cn](mailto:zhusn@nju.edu.cn)

Received 25 November 2021, revised 10 February 2022

Accepted for publication 2 March 2022

Published 1 April 2022



## Abstract

As a promising flat optical element, metasurfaces possess the powerful ability to manipulate chromatic dispersion, resulting in achromatic imaging, ultracompact spectrometers, and wavelength-dependent multifunctional nano-devices. However, conventional chromatic metalenses are incapable of arbitrarily tailoring dispersion within different bandwidths. Here, with a supercell composed of two nanostructures, we can arbitrarily control the chromatic dispersion of the metalens by using the phase differential equation and genetic optimization. We design three metalenses to verify the simultaneous tailoring of different chromatic dispersions in dual bands, which exhibits stronger chromatic dispersion manipulation capability compared with a single-structure-cell-based metalens. Our approach paves a new way for dispersion engineering of metalenses with potential applications in spectral imaging and material analysis.

Supplementary material for this article is available [online](#)

Keywords: metasurface, chromatic dispersion, super dispersion, light-field manipulation

(Some figures may appear in color only in the online journal)

## 1. Introduction

The acquisition of spectral information through the dispersion of light is non-trivial and imperative, has tremendous potential (including temperature detection, material composition analysis [1, 2], and exoplanet detection [3]), and has always triggered scientists to better understand nature and develop photonic technologies. Generally, high spectral resolution necessitates a huge dispersion effect to decompose the polychromatic light into patterns arranged in order of wavelength [4]. Conventional spectral systems integrated by thousands of spectrometers cannot achieve one-snapshot imaging with spatial real-time spectral information due to their bulky volume and complex configurations. Metasurfaces, consisting of an

array of nano-antennae in an ultrathin interface, have played a sensational role in nanophotonics during the past decade and enable steering of the phase, amplitude, and polarization of light [5–10] with abundant applications in imaging [11–13], displaying [14–18], optical tweezers [19, 20], quantum sources [21, 22], etc. As a ramification of metasurfaces, metalenses with dispersion engineering are primarily focused on eliminating chromatic aberration [23, 24] or highly extending the dispersion [25] in a continuous bandwidth; this is the focus of spectroscopic research, which aims to implement micro-nano spectrometers and spectral imaging devices with the aforementioned functionalities [26–35]. However, since every unit cell in the library presents a linear relation with the reciprocal of the wavelength, thereby such metalenses may lose the flexibility of tailoring phase profiles in different bands. In this regard, a multi-layer metalens is one of the most critical pieces in the puzzle [36–38]; in parallel, achieving on-demand

\* Authors to whom any correspondence should be addressed.

multitasking functionalities in different spectral domains with a single-layer metasurface is also necessary for the expansion of dispersion engineering.

In this work, we reveal highly controllable chromatic dispersion by specially designing supercell-based meta-atoms on single-layer metasurfaces. We firstly design a normal chromatic dispersive metasurface based on a unit-cell with a certain lateral shift along the transverse direction in the visible and infrared spectrum (485–1000 nm). Moreover, the supercell-based metasurface is applied to regulate the shift in the transverse direction of output light for the boundaries of adjacent bandwidths (485–630 nm and 730–1000 nm). Our approach is a further extension of chromatic dispersion engineering in flat optics for developing advanced applications in spectral imaging.

## 2. Principle and design

Figure 1(a) illustrates a schematic diagram of normal and controllable super chromatic dispersive metasurfaces through tailoring the focal positions for selected bandwidths at a fixed focal plane. For a highly dispersive metasurface composed by single meta-atoms, the phase profile of the metasurface at an arbitrary point in the focal plane  $(x', y', f)$  can be expressed as follows:

$$\varphi(x, y, \lambda) = -\frac{2\pi}{\lambda} \left( \sqrt{(x-x')^2 + (y-y')^2 + f^2} - \sqrt{(x')^2 + (y')^2 + f^2} \right), \quad (1)$$

where  $(x, y)$  denotes the coordinate of each meta-atom on the metasurface,  $f$  represents the focal length, and  $\lambda$  is the wavelength of the incident plane wave. Here, we set the working bandwidth as  $\lambda \in \{485, 1000 \text{ nm}\}$ , which covers from the visible to the infrared region. Figures 1(b) and (c) depict the side and top views of a unit cell based on a gallium nitride (GaN) meta-atom standing on a sapphire ( $\text{Al}_2\text{O}_3$ ) substrate (details of the refractive index can be found in supplementary figure S1 (available online at [stacks.iop.org/JPhysD/55/255105/mmedia](https://stacks.iop.org/JPhysD/55/255105/mmedia)) and several special values for readers as dots in the figure) with varying width  $W_0$ , length  $L_0$ , and rotation angle  $\theta$  as well as the fixed height  $H = 1.5 \mu\text{m}$  and lattice constants  $P_x = P_y = 320 \text{ nm}$ , respectively. In order to realize a highly chromatic dispersion with a large lateral shift at different wavelengths, the phase differential equation based on our previous work has to be mentioned [23, 24]. That is, for a normal chromatic dispersive metasurface at a continuous bandwidth  $\lambda \in \{\lambda_{11}, \lambda_{22}\}$ , exploiting the geometric phase by changing the rotation angle is adopted to satisfy a focusing function, and the introduced compensation phase  $\phi_{\text{shift}} = \max|\varphi_2 - \varphi_1|$ , determined by the propagation phase between the band boundaries  $\lambda_{11}$  and  $\lambda_{22}$  can achieve a large lateral shift with different incident wavelengths, which is calculated as:

$$\Delta\varphi(x) = \varphi(x_1, 0, \lambda_{11}) - \varphi(x_2, 0, \lambda_{22}) + \phi_{\text{shift}}. \quad (2)$$

However, a controllable chromatic dispersive metasurface, i.e. a library of supercells containing multiple meta-atoms in an individual lattice, should be required, for the reason that a unit cell composed of a single nanostructure in the pioneering works is not capable of controlling the dispersion arbitrarily in multiple and continuous bandwidths. By considering the non-local effects of the optical coupling between meta-atoms, the design and simulation can be operated directly [33, 39, 40]. In this work, two elliptical nanopillars with varying shapes are chosen to combine as a supercell attributed to the advantage of more degrees of freedom with six variables  $\{W_1, L_1, W_2, L_2, a, \theta\}$  to fulfill the phase space in the library, the side and top views of which are shown in figures 1(d) and (e). The period of a supercell is  $P_x' = P_y' = 400 \text{ nm}$  with the fixed height  $H = 1.5 \mu\text{m}$ . Figure 1(g) depicts the simulated phase values (blue filled circles) and the corresponding transmission (red line) for a supercell, exhibiting two independent approximately linear relations with the reciprocal of the wavelength in dual-band regions. Note that the phase diagram of the supercell-based nanostructure can be linearly fitted (green line) separately for two different ranges from 485 to 630 nm and 730–1000 nm. Apparently, the distinguished slopes of the fitting lines indicate that the supercell will show different relations with the wavelength within two bands, resulting in an abnormal optical effect. According to the above-mentioned discussion, the working band  $\{\lambda_1 - \lambda_2, \lambda_3 - \lambda_4\}$  will be divided into two independent bandwidths as  $\{\lambda_1, \lambda_2\}$  and  $\{\lambda_3, \lambda_4\}$ ; therefore, the respective chromatic dispersive characteristics in two different bandwidths requires three phase separate compensation phases as:

$$\begin{cases} \Delta\varphi_1(x) = \varphi(x'_1, 0, \lambda_1) - \varphi(x'_2, 0, \lambda_2) + \phi_{\text{shift1}}, \\ \Delta\varphi_2(x) = \varphi(x'_2, 0, \lambda_2) - \varphi(x'_3, 0, \lambda_3) + \phi_{\text{shift2}}, \\ \Delta\varphi_3(x) = \varphi(x'_3, 0, \lambda_3) - \varphi(x'_4, 0, \lambda_4) + \phi_{\text{shift3}}, \end{cases} \quad (3)$$

where the variable  $\{x'_1, x'_2, x'_3, x'_4, \phi_{\text{shift1}}, \phi_{\text{shift2}}, \phi_{\text{shift3}}\}$  should be properly established with the supercell to achieve the required chromatic dispersion. Here, the boundaries of two bandwidths are fixed at  $\lambda_1 = 485 \text{ nm}$ ,  $\lambda_2 = 630 \text{ nm}$ ,  $\lambda_3 = 730 \text{ nm}$ , and  $\lambda_4 = 1000 \text{ nm}$  within the designed center wavelength as 582.5 and 865 nm. Figure 1(f) depicts three metasurfaces designed to numerically demonstrate our method of intuitively manipulating the chromatic dispersion. Metasurface 1 holds the normal chromatic dispersion with bandwidths from 485 to 1000 nm. However, keeping the same transverse position at 485 and 1000 nm as metasurface 1, metasurface 2 performs a steerable chromatic dispersion with transverse shifts  $x_{21}$  and  $x_{22}$  at the boundary of two wavelength bands at 630 and 730 nm, respectively. As a result, the normal transverse distance is broken and the focal position along the transverse direction can be controlled at will. Metasurface 3 possesses a fixed focal point the same as metasurface 1 at the inner boundary of the dual-band (630 and 730 nm) and the tailored transverse focal position at the outer wavelength (485 and 1000 nm) to achieve the abnormal transverse shifts  $x_{31}$  and  $x_{32}$ .

According to the aforementioned discussion, a supercell-based phase library was created containing variable  $W_1, W_2$  from 40 to 120 nm and  $L_1, L_2$  from 60 to 340 nm with

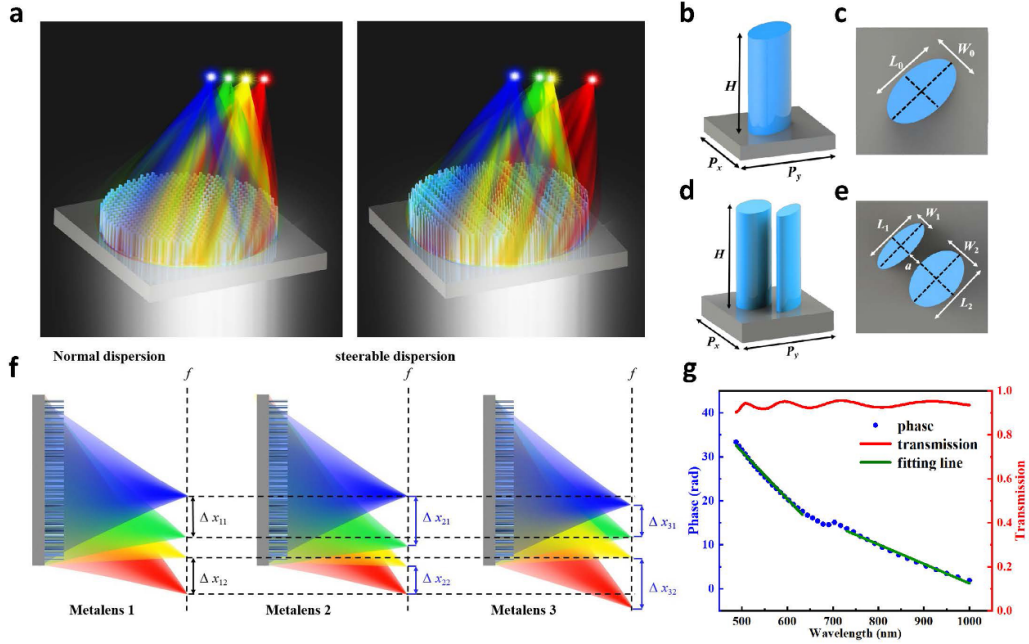


**Figure 1.** (a) Schematic diagram for normal (left) and steerable (right) super chromatic dispersive metalenses. In the case of the normal super chromatic dispersion, a lateral shift was set to naturally separate the output position of the different incident wavelengths at the same focal length. The focal point position will be tuned at the stated incident wavelengths for the case of manual controllable super chromatic dispersion. (b)–(e) The geometries of the unit-atom for the normal super chromatic dispersive metalens and the supercell for the manual steerable super chromatic dispersive metalens. (f) Schematic diagram of the different focal points in the  $x$ -direction for two bandwidth regions (485–630 nm and 730–1000 nm). (g) Simulated and fitting result of a typical supercell ( $W_1 = 90$  nm,  $L_1 = 60$  nm,  $W_2 = 80$  nm,  $L_2 = 120$  nm,  $a = 60$  nm).

20 nm increments of each geometric variable with a distance  $a = 60$  nm between two nanopillars in order to provide diverse phase dispersions using the commercial software Lumerical FDTD Solutions. The periodical boundary conditions are applied along the  $x$ - and  $y$ - axes and the perfectly matched layers (PMLs) are applied to in the  $z$ -direction. Therefore, the nonlocal coupling of the meta-atoms can be ignored, and the normalized magnetic energy density distribution of the coupled nanopillars is shown in supplementary figure S2. In the simulation area, the mesh accuracy of 2 is adopted and the minimum mesh step is set as 0.0002. Finally, left-hand circularly polarized light is used and the orthogonal polarized electric field can be obtained from the monitor. To deploy target metalenses with suitable supercell nanostructures, the optimization of a genetic algorithm can be introduced to select appropriate variables  $\{x'_1, x'_2, x'_3, x'_4, \phi_{shift1}, \phi_{shift2}, \phi_{shift3}\}$  to better fulfill the steerable chromatic dispersive requirement [31, 41–43], whose best matching is accomplished by iterative optimization such as selection, crossover, and mutation, and hence requires a defined residual function  $R_i$  to evaluate the results. Here,  $R_i$  can be set as the difference between the phase  $\Delta\varphi_{real}(x)$  in the phase library and the desired phase profile  $\Delta\varphi_i(x)$ , shown as:

$$R_i = \sum_{i=1}^n \left| e^{i\Delta\varphi_{real}(x)} - e^{i\Delta\varphi_i(x)} \right|. \quad (4)$$

And the fitness function  $F$  as the judgment basis of the genetic algorithm to achieve a better parameter group and the corresponding supercell distribution can be written as:

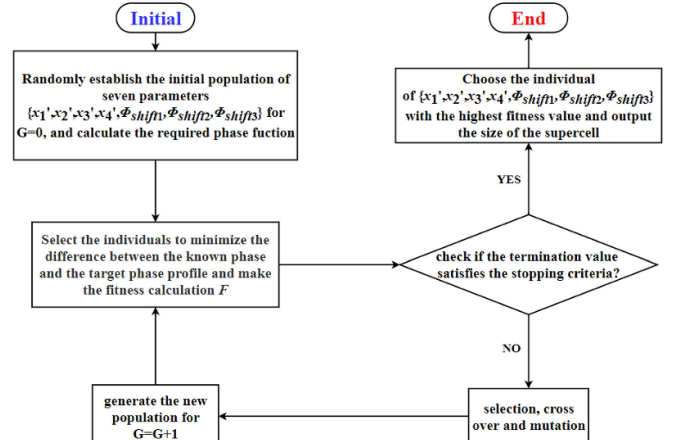


**Figure 2.** Flowchart of genetic algorithm optimization used to design our metalens.

$$F = \sum_{j=1}^N \sum_{i=1}^n \left| e^{i\varphi_{real}(\vec{x}, \vec{y}, \lambda_i)} - e^{i[\varphi_i(\vec{x}, \vec{y}, \lambda_i) + \phi_{shift}(\lambda_i)]} \right|, \quad (5)$$

where  $N$  is the number of supercells on the metasurface related to the lattice period and metasurface diameter and  $n$  is the number of calculated wavelengths. Figure 2(a) shows a flowchart of the genetic optimization; the ultimate parameter group after optimization is used to select the suitable supercell distribution. More details about genetic optimization can be found in supplementary S3.

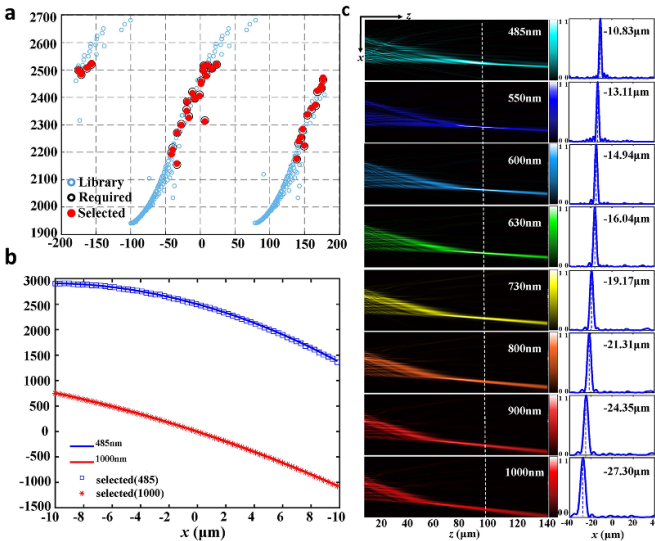


**Figure 3.** Simulated result for metalens 1. (a) The simulated phase at  $\lambda_1$  and the compensation phase between 485 and 1000 nm ( $\Delta\varphi \in [485, 1000] \text{ nm}$ ) for all individual structures based on a single nanopillar. The blue circles represent all the simulated results and the black circles denote the required compensation phase for the target function. (b) The required phase and the simulated phase of the selected nanostructures for functional metalenses at the two interested wavelengths. (c) The simulated result at different wavelengths. In particular, the focal plane ( $f = 100 \mu\text{m}$ ) is marked with a white dashed line and the normalized intensities at the working region are shown in the right set.

### 3. Result and discussion

For proof of concept, a super chromatic dispersive metalens (metalens 1) has been demonstrated with a radius  $R = 10 \mu\text{m}$  and  $\text{NA} = 0.1$  at a working region from 485 to 1000 nm. Among them, transverse shifts for the boundary of the bandwidth are set as  $x_1 = -10.8 \mu\text{m}$  and  $x_2 = -27.3 \mu\text{m}$  for metalens 1, respectively. Thereafter, many more nanoellipsoid structures with different combinations of long and short axes are simulated, with the phases imparted for the compensation phase  $\varphi$  and the maximum (1000 nm) wavelengths, as shown in figure 3(a) (blue circles). The black circles are the theoretical value for the expectation and the red dots represent the selected nanostructures, which have the smallest distance to the required phase profile. After completing all the calculations, we get the selected result of the phase profile at the maximum and minimum wavelengths (red asterisks and blue squares), as displayed in figure 3(b), exhibiting great agreement with the required phase lines. To confirm the performance of chromatic dispersion, metalens 1 is simulated with left-hand circularly polarization incidence. Figure 3(c) shows the simulated result of the normalized intensity profiles of the left-hand circularly output light at different wavelengths, and the corresponding normalized intensity distribution of the longitudinal cross sections in the focal plane ( $z = 100 \mu\text{m}$ ) is shown in the right inset.

To compare the dispersion for metalens 1–3 intuitively, the steerable super chromatic dispersive metalenses with the same radius  $R = 10 \mu\text{m}$ , a designed focal length

$f = 100 \mu\text{m}$ , and  $\text{NA} = 0.1$  within the working band {485–630 nm, 730–1000 nm} have been numerically demonstrated. Figure 4(a) apparently displays the library of compensation phases at three independent bandwidths during the optimization, which are marked as blue circles. However, in practice, the error in transmission of the library also needs to be considered; the elements with more than 60% efficiencies, marked as green circles, are chosen to prepare for acquiring better simulation results. For a vivid visualization, the required theoretical compensation phase points obtained from equation (3) of the ultimate parameter group are marked as black dots, and the selected supercells are marked as red dots after the optimization. Figure 4(b) gives information about the comparison of the target and selected phase profile for metalens 2 and 3 at four desired wavelengths. Among them, the lines represent the target phase and different geometric shapes show the phases of the selected elements, indicating they are well-fitted. Then, the selected supercells should be filled at each position on the metalenses with specific rotation angles followed by  $\theta = \varphi_{\max}/2$ , where  $\varphi_{\max}$  is the phase profile with the maximum wavelength incidence.

According to the simulated result for metalens 1, the transverse shifts  $x_{\lambda 1} = -10.83 \mu\text{m}$  and  $x_{\lambda 4} = -27.3 \mu\text{m}$  are fixed for metalens 2,  $x_{\lambda 2} = -17.5 \mu\text{m}$  and  $x_{\lambda 3} = -20 \mu\text{m}$  are controlled by selected supercells with genetic optimization, and the results are displayed on the left of figure 4(c) (supplementary table S1). For metalens 3 with fixed  $x_{\lambda 2} = 16.04 \mu\text{m}$  and  $x_{\lambda 3} = -19.17 \mu\text{m}$ ,  $x_{\lambda 1} = -12.6 \mu\text{m}$  and  $x_{\lambda 4} = -28.3 \mu\text{m}$  are tailored after genetic optimization, aiming to further manipulate the chromatic dispersion. The simulated transverse shifts and corresponding full widths at half maximum (FWHMs) are calculated and visualized in table 1, which are in agreement with our results. Also, a comparison of normal and manually controllable chromatic dispersive metalenses is provided and depicted in figures 5(a) and (b). The black squares exhibit a normal super chromatic effect when the transverse shift is gradually deviated from the optical axis when the wavelength raises, implying a linear relation with the wavelength, while metalens 2 and 3, represented by green filled circles and blue triangles, indicate that the dispersive relation splits into two parts that are completely different from metalens 1, proving that the rules of normal transverse shift are broken. Figures 5(c) and (d) illustrate the comparison of calculated efficiencies (defined as the ratio of the intensity of the output region of three times the FWHM centered at the focal position to the intensity passing through the metalens [44]); the highest efficiencies can be up to 57%, 46%, and 40%, respectively. Here, we select a suitable parameter only for simulated demonstration. Subsequently, three phase separate compensation phases ( $\Delta\varphi_1 \in [\lambda_1, \lambda_2]$ ,  $\Delta\varphi_2 \in [\lambda_2, \lambda_3]$  and  $\Delta\varphi_3 \in [\lambda_3, \lambda_4]$ ) with different radius  $R$  at the fixed focal length  $f = 100 \mu\text{m}$  and the tuned focal length  $f$  at the fixed radius  $R = 10 \mu\text{m}$  are shown in figures 5(e) and (f). Obviously, the three required compensation phases expand as the radius  $R$  increases and the focal length  $f$  decreases. It is theoretically possible to design metalenses of larger sizes that follow the rules shown in figures 5(e) and (f).

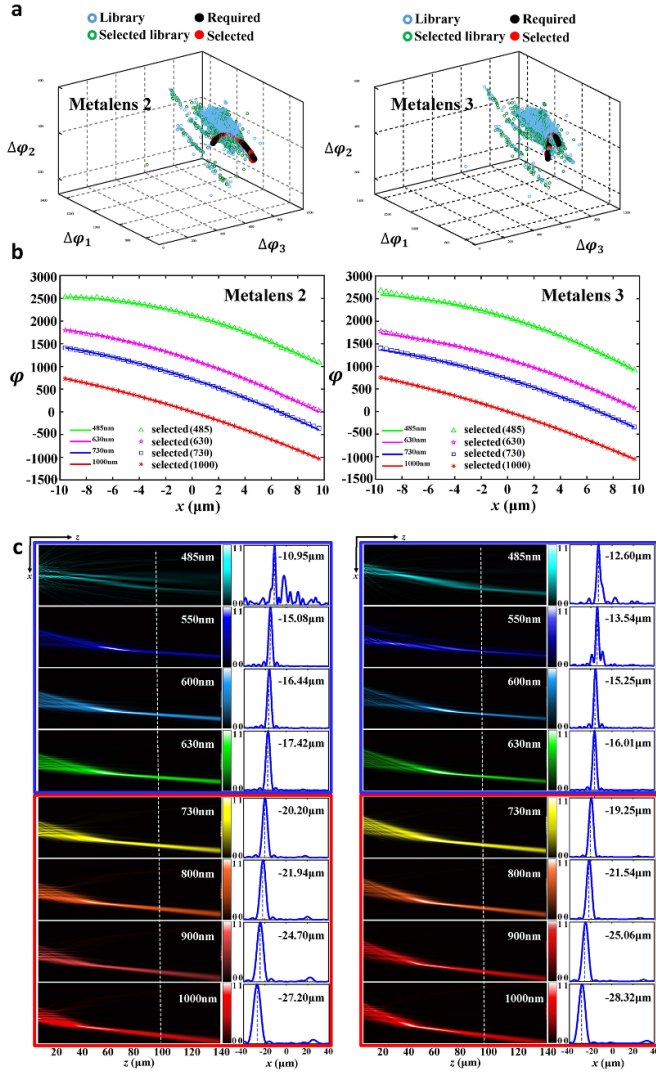


**Figure 4.** Results of optimization and simulation for metalens 2 and metalens 3. (a) The compensation phase at three bandwidths ( $\Delta\varphi_1$ ,  $\epsilon[\lambda_1, \lambda_2]$ ,  $\Delta\varphi_2$ ,  $\epsilon[\lambda_2, \lambda_3]$  and  $\Delta\varphi_3$ ,  $\epsilon[\lambda_3, \lambda_4]$ ) according to equation (2) for the library. The blue circles denote all the simulated elements and the green circles represent the elements with an average efficiency of more than 60%. The black dots locate the compensation target phase at each band for the functional metalens and the selected supercells that have the shortest sum distances to the black dots in the library are marked as red dots. (b) The target phase and the phase of simulated selected supercells for functional metalenses at four design wavelengths. (c) The simulated results at dual-bandwidths (485–630 nm and 730–1000 nm). In addition, the white dashed lines denote the focal length ( $f = 100 \mu\text{m}$ ) at the working region of each lens. The normalized intensity distributions and the transverse shift at the focal plane are shown with the changing of the wavelength in the right set.

**Table 1.** Calculated transverse shifts and FWHMs of simulated metalens samples.

Wavelength ( $\mu\text{m}$ )		0.485	0.55	0.6	0.63	0.73	0.8	0.9	1
Transverse shift ( $\mu\text{m}$ )	Metalens 1	10.83	13.11	14.94	16.04	19.17	21.31	24.35	27.3
	Metalens 2	10.95	15.08	16.44	17.42	20.2	21.94	24.7	27.2
	Metalens 3	12.6	13.54	15.25	16.01	19.25	21.54	25.06	28.32
FWHM ( $\mu\text{m}$ )	Metalens 1	2.92	2.42	2.76	3.16	3.65	4.15	4.86	5.39
	Metalens 2	2.77	3.85	4.08	4.93	5.83	6.39	7.02	7.99
Metalens 3	Metalens 3	2.68	3.3	3.6	4.3	5.26	5.91	6.72	7.79

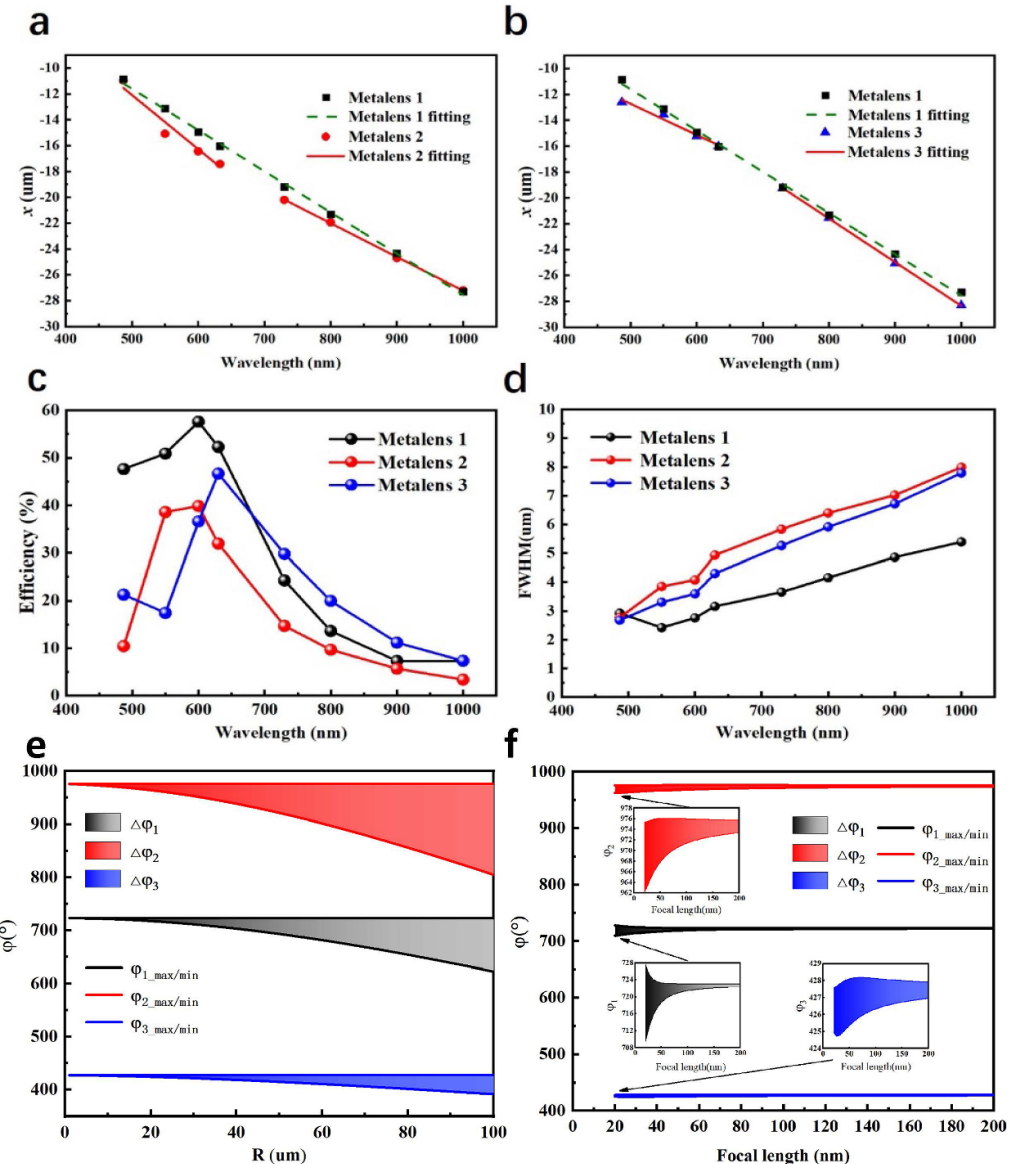


**Figure 5.** (a), (b) Comparison of output position with respect to wavelength between metalens 1 and 2 and between metalens 1 and 3, respectively. (c) Focusing efficiencies of the three metaleenses demonstrated. (d) FWHM of focal spots for the three samples. (e), (f) The calculated result of the compensation phase at three bandwidths (e) with the increasing radius  $R$  at the fixed focal length  $f = 100 \mu\text{m}$  and (f) the increasing focal length  $f$  at the fixed radius  $R = 10 \mu\text{m}$ .

#### 4. Conclusion

In summary, we combine the phase differential equation and genetic optimization to reveal normal and manually controllable super chromatic dispersion within continuous bandwidths based on metaleenses in the visible and infrared regime. Among these demonstrations, a normal chromatic dispersion effect is linear, related to the increasing wavelength on metalens 1; however, the rule can be broken on metalens 2 and 3 by specially designed supercell-based nanostructures with two independent linear relations with the reciprocal of the wavelength in dual-bandwidths, the transverse shift of which is steerable and proved to be different from metalens 1. We envision our approach can be utilized in dispersion-engineering

applications like compact and portable spectral classification and recognition when multiple materials in the field of view have different characteristic bands.

#### Data availability statement

All data that support the findings of this study are included within the article (and any supplementary files).

#### Acknowledgments

The authors are grateful for help from Run Chen, Jun Liu, Ruoyu Lin, Yifa Wu, Guangxing Gong, Xiaoshu Zhu,

Mengjing Xu, Qianhui Bi, Mengjiao Liu, Qin Ge, Juanzi He, and Mingqian Shi.

## Funding

The authors acknowledge financial support from the National Program on Key Basic Research Project of China (2017YFA0303700) and the National Natural Science Foundation of China (Nos. 11621091, 11822406, 11834007, 11774164, 11774162). This work is also supported by the Fundamental Research Funds for the Central Universities No. 020414380175.

## ORCID iDs

Boyan Fu  <https://orcid.org/0000-0001-6428-8080>  
 Tianyue Li  <https://orcid.org/0000-0001-7682-7483>  
 Shuming Wang  <https://orcid.org/0000-0002-0191-407X>

## References

- [1] Dean N 2015 Colouring at the nanoscale *Nat. Nanotechnol.* **10** 15–16
- [2] Wang P and Menon R 2015 Ultra-high-sensitivity color imaging via a transparent diffractive-filter array and computational optics *Optica* **2** 933–9
- [3] Wu Y, Chen S, Wang P, Zhou S, Feng Y, Zhang W and Wei R 2021 Simulation and analysis of the coherent-dispersion spectrometer for exoplanet detection *Mon. Not. R. Astron. Soc.* **503** 3032–43
- [4] Saleh B E A and Teich M C 2007 *Fundamentals of Photonics* 2nd edn (New York: Wiley)
- [5] Arbabi A, Horie Y, Bagheri M and Faraon A 2015 Dielectric metasurfaces for complete control of phase and polarization with subwavelength spatial resolution and high transmission *Nat. Nanotechnol.* **10** 937–43
- [6] Chen X, Huang L, Mühlenernd H, Li G, Bai B, Tan Q, Jin G, Qiu C-W, Zhang S and Zentgraf T 2012 Dual-polarity plasmonic metalens for visible light *Nat. Commun.* **3** 1198
- [7] Sun S, He Q, Xiao S, Xu Q, Li X and Zhou L 2012 Gradient-index meta-surfaces as a bridge linking propagating waves and surface waves *Nat. Mater.* **11** 426–31
- [8] Yu N, Genevet P, Kats M A, Aieta F, Tetienne J-P, Capasso F and Gaburro Z 2011 Light propagation with phase discontinuities: generalized laws of reflection and refraction *Science* **334** 333–7
- [9] Li S, Li X, Wang G, Liu S, Zhang L, Zeng C, Wang L, Sun Q, Zhao W and Zhang W 2019 Multidimensional manipulation of photonic spin Hall effect with a single-layer dielectric metasurface *Adv. Opt. Mater.* **7** 1801365
- [10] Li T, Li X, Yan S, Xu X, Wang S, Yao B, Wang Z and Zhu S 2021 Generation and conversion dynamics of dual Bessel beams with a photonic spin-dependent dielectric metasurface *Phys. Rev. Appl.* **15**
- [11] Huo P et al 2020 Photonic spin-multiplexing metasurface for switchable spiral phase contrast imaging *Nano Lett.* **20** 2791–8
- [12] Khorasaninejad M, Chen W T, Devlin R C, Oh J, Zhu A Y and Capasso F 2016 Metalenses at visible wavelengths: diffraction-limited focusing and subwavelength resolution imaging *Science* **352** 1190–4
- [13] Luo Y et al 2021 Varifocal metalens for optical sectioning fluorescence microscopy *Nano Lett.* **21** 5133–42
- [14] Bao Y, Wen L, Chen Q, Qiu C-W and Li B 2021 Toward the capacity limit of 2D planar Jones matrix with a single-layer metasurface *Sci. Adv.* **7** eabb0365
- [15] Deng Z-L, Tu Q-A, Wang Y, Wang Z-Q, Shi T, Feng Z, Qiao X-C, Wang G P, Xiao S and Li X 2021 Vectorial compound metapixels for arbitrary nonorthogonal polarization steganography *Adv. Mater.* **33** 2103472
- [16] Fan Q et al 2020 Independent amplitude control of arbitrary orthogonal states of polarization via dielectric metasurfaces *Phys. Rev. Lett.* **125** 267402
- [17] Huang L et al 2013 Three-dimensional optical holography using a plasmonic metasurface *Nat. Commun.* **4** 2808
- [18] Zheng G, Mühlenernd H, Kenney M, Li G, Zentgraf T and Zhang S 2015 Metasurface holograms reaching 80% efficiency *Nat. Nanotechnol.* **10** 308–12
- [19] Li T, Xu X, Fu B, Wang S, Li B, Wang Z and Zhu S 2021 Integrating the optical tweezers and spanner onto an individual single-layer metasurface *Photon. Res.* **9** 1062–8
- [20] Zhu L et al 2020 A dielectric metasurface optical chip for the generation of cold atoms *Sci. Adv.* **6** eabb6667
- [21] Bao Y, Lin Q, Su R, Zhou Z-K, Song J, Li J and Wang X-H 2020 On-demand spin-state manipulation of single-photon emission from quantum dot integrated with metasurface *Sci. Adv.* **6** eaba8761
- [22] Li L et al 2020 Metalens-array-based high-dimensional and multiphoton quantum source *Science* **368** 1487–90
- [23] Wang S et al 2018 A broadband achromatic metalens in the visible *Nat. Nanotechnol.* **13** 227–32
- [24] Wang S et al 2017 Broadband achromatic optical metasurface devices *Nat. Commun.* **8** 187
- [25] Chen C et al 2019 Spectral tomographic imaging with aplanatic metalens *Light Sci. Appl.* **8** 99
- [26] Chen W T, Zhu A Y, Sanjeev V, Khorasaninejad M, Shi Z, Lee E and Capasso F 2018 A broadband achromatic metalens for focusing and imaging in the visible *Nat. Nanotechnol.* **13** 220–6
- [27] Shi Z et al 2018 Single-layer metasurface with controllable multiwavelength functions *Nano Lett.* **18** 2420–7
- [28] Lu X, Guo Y, Pu M, Zhang Y, Li Z, Li X, Ma X and Luo X 2021 Broadband achromatic metasurfaces for sub-diffraction focusing in the visible *Opt. Express* **29** 5947–58
- [29] Nda A, Hsu L, Ha J, Park J-H, Chang-Hasnain C and Kanté B 2020 Octave bandwidth photonic fishnet-achromatic-metalens *Nat. Commun.* **11** 3205
- [30] Ou K et al 2021 Broadband achromatic metalens in mid-wavelength infrared *Laser Photonics Rev.* **15** 2100020
- [31] Ren J, Li T, Fu B, Wang S, Wang Z and Zhu S 2021 Wavelength-dependent multifunctional metalens devices via genetic optimization *Opt. Mater. Express* **11** 3908–16
- [32] Shrestha S, Overvig A C, Lu M, Stein A and Yu N 2018 Broadband achromatic dielectric metalenses *Light Sci. Appl.* **7** 85
- [33] Sisler J, Chen W T, Zhu A Y and Capasso F 2020 Controlling dispersion in multifunctional metasurfaces *APL Photonics* **5** 056107
- [34] Wang Y et al 2021 High-efficiency broadband achromatic metalens for near-IR biological imaging window *Nat. Commun.* **12** 5560
- [35] Zhu A Y, Chen W T, Sisler J, Yousef K M A, Lee E, Huang Y-W, Qiu C-W and Capasso F 2019 Compact aberration-corrected spectrometers in the visible using dispersion-tailored metasurfaces *Adv. Opt. Mater.* **7** 1801144
- [36] Mansouree M, Kwon H, Arbabi E, McClung A, Faraon A and Arbabi A 2020 Multifunctional 2.5D metastructures enabled by adjoint optimization *Optica* **7** 77–84
- [37] Zhou Y, Kravchenko I I, Wang H, Nolen J R, Gu G and Valentine J 2018 Multilayer noninteracting dielectric

- metasurfaces for multiwavelength metaoptics *Nano Lett.* **18** 7529–37
- [38] Zhou Y, Kravchenko I I, Wang H, Zheng H, Gu G and Valentine J 2019 Multifunctional metaoptics based on bilayer metasurfaces *Light Sci. Appl.* **8** 80
- [39] Chen W T, Zhu A Y, Sisler J, Bharwani Z and Capasso F 2019 A broadband achromatic polarization-insensitive metalens consisting of anisotropic nanostructures *Nat. Commun.* **10** 355
- [40] Spägle C, Tamagnone M, Kazakov D, Ossiander M, Piccardo M and Capasso F 2021 Multifunctional wide-angle optics and lasing based on supercell metasurfaces *Nat. Commun.* **12** 3787
- [41] Huntington M D, Lauhon L J and Odom T W 2014 Subwavelength lattice optics by evolutionary design *Nano Lett.* **14** 7195–200
- [42] Liu Z, Liu X, Xiao Z, Lu C, Wang H-Q, Wu Y, Hu X, Liu Y-C, Zhang H and Zhang X 2019 Integrated nanophotonic wavelength router based on an intelligent algorithm *Optica* **6** 1367–73
- [43] Goldberg D E 1989 *Genetic Algorithms in Search, Optimization, and Machine Learning* (Boston, MA: Addison-Wesley Longman Publishing)
- [44] Li H, Xiao X, Fang B, Gao S, Wang Z, Chen C, Zhao Y, Zhu S and Li T 2021 Bandpass-filter-integrated multiwavelength achromatic metalens *Photon. Res.* **9** 1384–90